

Chemically-induced Neurite-like Outgrowth Reveals Multicellular Network Function in Patient-derived Glioblastoma Cells

Barbara da Silva¹, Bronwyn K. Irving¹, Euan S. Polson¹, Alastair Droop^{1,2}, Hollie B.S. Griffiths³, Ryan K. Mathew^{1,4}, Lucy F. Stead¹, Joanne Marrison⁵, Courtney Williams³, Jennifer Williams¹, Susan C. Short¹, Margherita Scarcia^{1,6}, Peter J. O'Toole⁵, Simon J. Allison³, Georgia Mavria¹, and Heiko Wurdak^{1,*}.

¹School of Medicine, University of Leeds, Leeds, LS2 9JT, UK

²Leeds Institute for Data Analytics, University of Leeds, Leeds, LS2 9JT, UK

³School of Applied Sciences, University of Huddersfield, Huddersfield, HD1 3DH, UK

⁴Department of Neurosurgery, Leeds General Infirmary, Leeds, LS1 3EX, UK

⁵Department of Biology, University of York, York, YO10 5DD, UK

⁶Present address, Faculty of Biology, Medicine and Health, University of Manchester, Manchester M13 9PT, UK

*Correspondence: h.wurdak@leeds.ac.uk

ABSTRACT

Tumor stem cells and malignant multicellular networks have been separately implicated in the therapeutic resistance of Glioblastoma Multiforme (GBM), the most aggressive type of brain cancer in adults. We show that small molecule inhibition of RHO-associated serine/threonine kinase (ROCKi) significantly promoted the outgrowth of neurite-like cell projections in cultures of heterogeneous patient-derived GBM stem-like cells. These projections formed *de novo*-induced cellular network (iNet) 'webs', which regressed after withdrawal of ROCKi. Connected cells within the iNet web exhibited long range calcium signal transmission, and significant lysosomal and mitochondrial trafficking. In contrast to their less-connected vehicle control counterparts, iNet cells remained viable and proliferative after high-dose radiation. These findings demonstrate a link between ROCKi-regulated cell projection dynamics and the formation of radiation-resistant multicellular networks. Our study identifies means to reversibly induce iNet webs *ex vivo*, and may thereby accelerate future studies into the biology of GBM cellular networks.

KEYWORDS

Brain tumor, glioblastoma multiforme, patient-derived tumor cells, GBM stem-like cells, ROCK inhibition, neurite-like outgrowth, malignant multicellular network, mitochondrial trafficking, radiation resistance

INTRODUCTION

GBM is the most frequent malignant primary brain tumor in adults and despite multimodality treatment, prognosis remains poor (Davis, 2016; Grossman and Batara, 2004). Five-year survival is <5% (Ostrom et al., 2014) and, despite surgical removal of the tumor bulk, GBM often recurs from residual tumor cells surviving radiation and chemotherapy (Osuka and Van Meir, 2017). The cellular response to these treatments likely involves the cytoskeleton, a key organizer of cell and organelle function, movement, and shape (Fletcher and Mullins, 2010). However, the molecular mechanisms underlying cytoskeletal dynamics in GBM cells remain largely elusive.

The RHO-associated serine/threonine kinase (ROCK) family plays a central role in the regulation of actin cytoskeletal dynamics (Sanz-Moreno et al., 2011). ROCK comprises the ROCK1 and ROCK2 proteins phosphorylating diverse downstream substrates that regulate actin filament stabilization and myosin-driven contraction, respectively (Maekawa et al., 1999; Ohashi et al., 2000; Rath and Olson, 2012). Accordingly, ATP-competitive small molecule inhibitors have been used to study the role of ROCK1 and ROCK2 in cells, and chemical pan-ROCK inhibition (hereinafter referred to as ROCKi) has been considered as a potential anti-tumor therapeutic strategy (Rath and Olson, 2012). While ROCKi promotes morphological changes in neural stem cells (Jia et al., 2016), axonal outgrowth, and neuroprotection (Dergham et al., 2002; Fournier et al., 2003; Fujita and Yamashita, 2014), conflicting pro- and anti-tumor effects have been reported in various cancer cell types (Salhia et al., 2005; Tilson et al., 2015; Zohrabian et al., 2009).

We hypothesized that ROCKi-dependent cytoskeletal rearrangements may affect the GBM cellular phenotype. We observed that ROCKi robustly induced the elongation of GBM cell projections that were morphologically akin to neurites. Furthermore, we investigated the impact of these cell projections on cellular connectivity and cooperation using mathematical and experimental network analysis and examined multicellular network function in regards with a potential for promoting radiation resistance (Winkler and Wick 2018; Osswald et al. 2015; Weil et al. 2017).

RESULTS AND DISCUSSION

ROCKi leads to neurite-like projection elongation in GBM cell models

We phenotypically characterized chemical ROCK inhibition in transcriptionally heterogeneous patient-derived GBM cell lines (GBM1, GBM4, GBM11, GBM13, GBM20) that represent different GBM subtypes (Polson et al., 2018). We used adherent culture conditions, which conserved their stem cell-like characteristics (da Silva et al., 2018; King et al., 2017; Polson et al., 2018; Wurdak, 2012; Wurdak et al., 2010), and ROCKi Y-27632, a biochemical tool for ROCK investigation (Rath and Olson, 2012). After stimulation of the RhoA/ROCK pathway in GBM1 cells with Lysophosphatidic acid (LPA; 1 μ M), Y-27632 (20 μ M) significantly reduced the level of phosphorylated ROCK downstream effector protein myosin phosphatase target subunit 1 (MYPT1) after 30 minutes at Thr853 (Garton et al., 2008) as compared to the vehicle (H₂O) control (Fig. S1A; phosphorylated MYPT1 protein levels

partially recovered after 4 hours suggesting compensatory upstream signaling). Time lapse microscopy of five different GBM cell models with 20 μM Y-27632 revealed a pronounced rapid elongation of cellular projections akin to cytokine-stimulated neurite outgrowth (Drubin et al., 1985) (**Video S1**). We determined the change in cellular projection length (CPL) for 21 randomly-selected individual cells per GBM cell model by subtracting the total projection lengths at t_0 from the values obtained for the same cells 24 hours after vehicle- or Y-27632 treatment. In the presence of Y-27632, the CPL was significantly elevated in all tested GBM cell models (compared to the vehicle (H_2O) controls; $p \leq 0.0002$; **Fig. 1A**). Projections stained positive for the neuron-specific neurite markers Class III β -tubulin (TuJ1) and the microtubule-associated protein 2 (MAP2) (**Fig. 1B**), which is expressed in both low- and high-grade diffuse brain tumors (Wharton et al., 2002). Maximal CPL values were reached after a treatment period of ~ 24 hours (**Fig. S1 B,C**). Expression of TuJ1 and MAP2 remained unaltered, indicating redistribution of cell body neurofilaments into the elongating projections (**Fig. S1D**).

Y-27632-treated cells consistently exhibited a marked CPL elongation in three different GBM cell models (**Fig. 1C**). The structurally-distinct ROCK inhibitors H1152 (10 μM ; (Ikenoya et al., 2002) and GSK269962 (5 μM ; (Doe et al., 2007) recapitulated the Y-27632 effect in GBM1 cells ($p < 0.0001$; **Fig. 1D**), linking ROCKi and the cellular phenotype. Two different downstream effectors of ROCK were disrupted using Blebbistatin, an inhibitor of the non-muscle myosin II protein (NM II; (Straight et al., 2003), and LIM domain kinase inhibitor 3 (LIMKi3), a suppressor of LIMK-dependent cofilin phosphorylation (Ross-Macdonald et al., 2008). Blebbistatin (2.5 μM) markedly increased the CPL ($p < 0.0001$), whereas LIMKi3 (5 μM) had little (control-like) effect, thus suggesting that disruption of ROCKi activation of NM II, rather than LIMK protein was relevant for the observed CPL elongation (**Fig. 1D**). GBM1 cell exposure to LPA (1 μM , 8 hours), which induces neurite retraction in neuronal cells (Kranenburg et al., 1999), did not reduce the CPL in presence of Y-27632 (**Fig. 1E**). Furthermore, culture of GBM cells in Matrigel, an extracellular matrix-based hydrogel, which can promote tube formation in cell lines (Francescone et al., 2011), was unable to mask the Y-27632-induced effect on neurite-like outgrowth (**Fig. 1F**).

A *de novo*-induced network (iNet) phenotype in GBM cells

To determine whether the ROCKi-induced projection elongations enabled an integrated multicellular system, we used mathematical network analysis through mapping GBM1 cell bodies and protrusions under the assumption that they are connected objects, equivalent to nodes and edges in a discrete network (Jackson et al., 2017) (**Fig. 2A**). In contrast to the control cell phenotype (hereinafter referred to as Con), the logical network topology indicators ‘degree and betweenness centrality’ (Newman, 2006) were significantly elevated in the Y-27632-treated cells (**Fig. 2B**), hence indicating a *de novo*-induced cellular network (hereinafter referred to as iNet). The iNet formation was accompanied by a marked decrease in cellular motility under $>50\%$ confluency, whereas motility remained unaltered when intercellular contact was minimal ($<10\%$ confluency; **Fig. 2C**). Moreover, iNet cells retracted their projections within eight hours of ROCKi withdrawal, demonstrating reversion of the cell ‘web’ phenotype (hereinafter referred to as Rev) (**Fig. 2D, Fig. S1E**). Time lapse microscopy (**Fig. 2E**), clonal cell growth analysis (**Fig. S1F**), and Ki67 stainings (**Fig. 2E, Fig. S2A**), indicated comparable proliferation capacities of Con, iNet, and Rev GBM1 cells. In addition, RNA-seq transcriptional comparison of iNet and Rev cellular profiles revealed Adhesion Molecule With Ig Like Domain 3 (AMIGO3), an

inhibitor of axonal growth (Ahmed et al., 2013), as the most downregulated iNet-associated transcript (**Fig. 2F**). Further analysis using The Database for Annotation, Visualization and Integrated Discovery (DAVID; (Huang et al., 2009a; Huang et al., 2009b) and Gene Set Enrichment Analysis (GSEA; Subramanian et al., 2005) suggested iNet-specific enrichment of axonal guidance-regulating genes (**Fig. S2B, C**), and positive iNet signature correlations with cell projection growth, cytoskeletal organization, cell cycle progression, and anti-apoptotic pathways (**Fig. 2G**).

The iNet phenotype increases GBM multicellular cooperation

To test whether iNet promoted multicellular cooperation, we assessed calcium and fluorescent dye transmission in GBM1 cells (**Fig. 3A and B**). Upon focused laser stimulation, fluorescence indicator of intracellular calcium 3 (Fluo-3; Minta et al., 1989) signal intensity increased in the neighboring cells, and maximum intensities were markedly elevated in iNet compared to Con cells ($p=0.012$; **Fig. 3C**). Less than 40% of Con cells participated in the Fluo-3 transmission waves with Fluo-3 signal angles ranging between 60 and 320 degrees (**Fig. 3D**). In contrast, ~80% of iNet cells participated in the calcium signal extensions exhibiting angles of >320 degrees (**Fig. 3D**). In addition, scrape-loading dye transfer experiments (el-Fouly et al., 1987) showed a significant increase in the cell-to-cell transfer of Lucifer yellow in iNet compared to Con conditions (>2 -fold, $p=0.005$; **Fig. 3E**), thus indicating gap junction-mediated cell-to-cell communication. Furthermore, confocal time lapse imaging revealed significant localization and trafficking of lysosomes and mitochondria into iNet cell projections, which was limited by the lack of neurite-like elongations in Con cells (**Fig. 3F and G, Videos S3-6**). We next carried out GBM1 co-culture (1:1) experiments with MitoTracker-labelled mitochondrial 'donor' and GFP-expressing 'recipient' cells (harboring unlabelled mitochondria). After 24 hours, the transfer of labelled mitochondria into recipient cells was significantly increased (≥ 2 -fold) by iNet in a cell density-dependent fashion (**Fig. 3H, I**). These results demonstrate an intercellular physical connection beyond mitochondrial trafficking to the cortical cytoskeleton, which has been shown to promote tumor cell motility/invasion (Caino et al., 2013), and metastasis (Caino et al., 2016).

The iNet phenotype promotes survival of GBM cells post radiation

To test whether iNet increased cellular stress resistance, we irradiated iNet, Con, and Rev GBM1 cells with 0, 2, 8, or 20 Gy, which resulted in a dose-dependent increase in DNA double-strand breaks as assessed by γ H2AX staining (Kuo and Yang, 2008) (**Fig. S3A,B**). In contrast to Con and Rev cells, the irradiated iNet cells exhibited a marked increase in cellular projection outgrowth (**Fig. S3C**), and proliferation/survival rates, which were corroborated by live cell confluency measurements (**Fig. 4A**), and cell fate analysis (tracing 15 individual cells per Con, Rev, and iNet condition using time lapse microscopy; **Fig. S3D**). Consistently, nuclear fragmentation was significantly reduced five days after radiation (2, 8, and 20 Gy) in iNet compared with Con and Rev cells (>2 -fold; $p<0.001$; **Fig. 4B**). Concomitantly, a dose-dependent increase in cytoplasmic swelling was observed in Con and Rev but not iNet cells (**Fig. 4C**).

Analysis of the iNet cells confirmed that the vast majority of nuclear fragmentation ($\geq 88\%$) appeared outside of the multicellular networks and within a cellular subpopulation ($<5\%$ of total cells) that remained unconnected (**Fig. S4A**). Luminescent cell viability assays indicated a marked sustainability of iNet cell survival/proliferation after 8 and 20 Gy radiation doses. In

agreement with glioma stem cell-associated radioresistance (Bao et al., 2006), only high-dose radiation (20 Gy) reduced GBM1 cell survival in Con and Rev conditions by approximately 50%, whereas the iNet cells remained viable ($p=0.0072$; **Fig. 4D**). Furthermore, mRNA-seq transcriptional profiling and GSEA comparing Rev and iNet cells post 20 Gy irradiation suggested positive iNet signature correlations with ‘mitotic cell cycle’, ‘negative regulation of cell death’, ‘P53’, ‘hypoxia’, and ‘oxidative stress’ pathways (**Fig. S4B**). Consistent with the latter being an expected consequence of ionizing radiation (Azzam et al., 2012), extracellular flux analysis 5 days after high-dose radiation (20 Gy) showed that basal oxygen consumption rate (OCR), and OCR following mitochondrial stress test, were significantly elevated in iNet, compared to Con and Rev conditions (**Fig. 4E**). This indicates an iNet phenotype-mediated ability of GBM cells to maintain their oxidative metabolism under radiation-induced stress.

In conclusion, our results show that ROCKi significantly promotes the outgrowth of cell projections in a spectrum of GBM stem-like models, which in turn enabled the *de novo* formation of cooperating multicellular networks. GBM stem-like cells have been shown to form interconnected networks through vasculogenic tubular structures (known as vasculogenic mimicry) based on endothelial-like differentiation in matrigel (El Hallani et al., 2010). However, we observed rapid evolvement of neurite-like networks via ROCKi treatment which was distinct from GBM cellular differentiation/trans-differentiation (Piccirillo et al. 2006; Wurdak et al. 2010; El Hallani et al., 2010). The iNet formation was characterized by chemical reversibility, unaltered proliferation, and a gene expression profile of cytoskeletal rearrangement implicating axonal outgrowth pathways. This induction of a reversible phenotypic switch for cellular networking may aid in the elucidation of intermittent cytoskeletal dynamics, and the exchange of cellular materials including mitochondria. Intercellular communication and mitochondrial transfer have been linked to increased cellular stress resistance and proliferation (Osswald et al., 2015; Torralba et al., 2016). Accordingly, iNet phenotypes may aid discovery and validation of radiosensitization targets in poorly-differentiated GBM cells. Further investigations may shed light onto the mechanistic link between ROCKi and GBM cell network morphologies and their organelle trafficking as well as tumor-promoting functions.

MATERIALS AND METHODS

Cell culture

The patient-derived GBM cell models were previously established and characterized as described in (Polson et al., 2018; Wurdak et al., 2010). The GBM1 (classical/proneural GBM subtype), GBM4 (mesenchymal GBM subtype), GBM11 (mesenchymal GBM subtype), GBM13 (proneural GBM subtype), and GBM20 (proneural/mesenchymal GBM subtype) cell lines represent a spectrum of transcriptionally-heterogeneous primary and recurrent tumors (Polson et al., 2018). All these cell models maintain stem cell-like characteristics under adherent culture conditions, hence allowing for the rapid quantification of cellular responses to chemical perturbations (da Silva et al., 2018; King et al., 2017; Polson et al., 2018; Wurdak, 2012; Wurdak et al., 2010). The cells were adherently propagated on plasticware coated with poly- L-ornithin (5 $\mu\text{g}/\text{mL}$, Sigma, P3655) and laminin (5 mg/mL , Invitrogen, 23017-015). The cells were cultured in Neurobasal medium (Gibco, 21103-049) supplemented with B27 (0.5x, Invitrogen, 17504-044), N2 (0.5x, Invitrogen, 17502-048), recombinant human basic fibroblast growth

factor (40 ng/mL, bFGF, Gibco, PHG0024) and epidermal growth factor (40 ng/mL, EGF, R&D systems, 236-EG). Cells were maintained in a humidified incubator with 5% CO₂ at 37 °C.

Small molecule inhibitor treatments

For small molecule inhibitor cell profiling, a seeding density of 20,000 cells per cm² was used and small molecule inhibitor treatments started post cell adhesion (overnight). The ROCK pathway inhibitors Y-27632 (20 μM, Sigma, Y0503), H1125 (10 μM, Tocris, 2141), GSK 269962 (5 μM, Tocris, 4009), Blebbistatin (2.5 μM, Tocris, 1853) and LIM kinase inhibitor (LIMKi3, a kind gift from Michael Olson, Ryerson University; 5 μM) were added for 24 hours. For compound withdrawal ('washout') experiments, cells were treated with distinct ROCK pathway inhibitors for the indicated period, followed by the removal of the treatment containing media (washing the cells with PBS), and subsequent addition of media lacking the small molecule inhibitors. Cells were assessed 8 hours post compound 'washout'.

Live cell imaging and cell confluency measurements

Live cell imaging was performed using GBM1 cells as previously described (Polson et al., 2018). Cells were seeded at a density of 20,000 cells per cm². Cells were treated with vehicle (H₂O) or Y-27632 (20 μM) and observed/recorded using the IncuCyte ZOOM® live cell imaging system (Essen Bioscience).

For cellular projection length (CPL) measurements, projections of random cells were measured at t_0 . Cells were then individually tracked for 24 hours after which the projections were measured again. CPL values were obtained by subtracting the measured length of t_0 from the length at t_{24} . For cells showing an increase in projection length after 24 hours this results in a positive CPL value, whilst a reduction in projection length results in a negative CPL value.

For confluency/growth curve analysis, the IncuCyte ZOOM® Confluence Processing analysis tool was used. For each condition, images were acquired longitudinally at set time points (t_0 , t_{25} , t_{50} , t_{100} , t_{150} ,) 25 hours, 50 hours, 100 hours, 150 hours) and these images were further processed by the IncuCyte ZOOM® Confluence Processing tool to quantify the increase in cellular density over background in each analyzed condition.

Clonal cell growth assay

Cells were seeded at a density of 150 cells/well into 24-well plates and allowed to adhere for 24 hours. The next day, the single cells in each well were identified and counted. Treatments were carried for 7 days using vehicle (H₂O) or Y-27632 (20 μM) or a compound 'washout' condition (via medium change after 16 hours of Y-27632 treatment). On day 3 all media were refreshed sustaining the distinct conditions until experimental endpoint at day 7. The number of clonally-derived colonies consisting of >4 cells were determined by phase contrast microscopy.

Immunostaining

Cells were fixed with 4% (w/v) paraformaldehyde (PFA, Sigma, P6148) for 10 minutes and blocking was carried out for 1 hour at room temperature with staining buffer (10% FBS in PBS) supplemented with 0.03% (v/v) Triton X-100 (Sigma, T8787). Next, the cells were incubated at 4°C overnight in staining buffer with the following primary antibodies: anti-neuronal class III β-tubulin (TuJ1, 1:300, Covance, 801202); anti-microtubule-associated protein 2 (MAP2, 1:1000, Abcam, ab5392); anti-Ki67 (1:200, Abcam, ab16667) and anti-phospho-H2AX (γH2AX, 1:800, Merck, JBW130). The cells were then incubated in staining buffer for 1

hour in the dark at room temperature with the following secondary antibodies: goat anti-mouse IgG with Alexa fluor 488 conjugate (1:500, Life technologies, A11029); goat anti-chicken IgG with Alexa fluor 647 conjugate (1:500, Life technologies, A21449), and Cy3 (1:500, Jackson ImmunoResearch, 711-165-152, conjugated). The fluorescence signal was detected using an EVOS digital inverted fluorescence microscope or Nikon A1R confocal microscope.

Immunoblotting

Whole-cell extracts were prepared by harvesting cells either in Laemmli sample buffer supplemented with 10 mM sodium fluoride, 1mM sodium vanadate, 10 mM sodium β -glycerophosphate, 0.5 mM PMSF and Complete-EDTA free protease inhibitor (Roche, Diagnostics GmbH), or in cell lysis buffer (Cell Signalling, 98035) supplemented with 1mM PMSF (Cell Signalling, 8553). Samples were sonicated for 15 seconds prior to centrifugation. Lysates were then loaded onto Mini-Protean TGX precast gels (4-15%, Biorad, 4561085 or 4561083) and resolved proteins transferred onto nitrocellulose membrane (0.45 μ m, Biorad, 9004-70-0). Membranes were exposed to the following antibodies: chicken anti-MAP2 (1:1000, Abcam, ab5392), mouse anti-TuJ1 (1:1000, Biolegend, 801202), rabbit anti-Phosphorylated MYPT1 (Thr853; 1:1000, Cell Signalling, 4156), rabbit anti-MYPT1 (1:1000, Cell Signalling, 2634) or mouse anti-b-actin (1:10000, Sigma, A1978). Fluorescent secondary antibodies used were goat anti-chicken IgG with Alexa fluor 647 conjugate (1:5000, Life technologies, A21449) or goat anti-mouse IgG with Alexa fluor 488 conjugate (1:5000, Life technologies, A11029). Fluorescence was detected using ChemiDoc MP Imaging System (BioRad) and quantified using ImageJ software. HRP secondary antibodies used were goat anti-mouse IgG with peroxidase conjugate (1:5000, Sigma, A4416) and goat anti-rabbit IgG with peroxidase conjugate (1:5000, Sigma, A6154) and detected using ECL prime detection reagent (Amersham, RPN2232).

Cell projection quantification using NeuriteTracer

Images of neurite-like projection formation were obtained as described above and subject to image analysis using the NeuriteTracer plugin for ImageJ (Fiji) (Pool et al., 2008). Threshold parameters were defined using the vehicle cells. The TuJ1 or MAP2-stained CPL (μ m) was calculated as follows: total projection outgrowth length (all cells) divided by the number of (DAPI-stained) nuclei. For CPL quantification, five different images (technical replicates) were analyzed per treatment for each independent experiment. On average each image encompassed ~40 cells.

LPA Treatment and matrigel network formation

Control and network phenotypes were established for 24 hours with treatment of vehicle (H_2O) or Y-27632 (20 μ M) in cells seeded at a density of 10,000 per cm^2 . Control cells were next treated with Oleoyl-L- α -Lysophosphatidic acid sodium salt (LPA, 1 μ M, Sigma, 22556-62-3). Network cells were subsequently treated with vehicle or LPA with and without Y-27632 (20 μ M). After 8 hours cells were fixed for 15 minutes with 4% (w/v) PFA. Cells underwent staining for TuJ1 and CPL quantification was performed for each experiment on 5 images per condition using the NeuriteTracer ImageJ plugin.

GFP-expressing GBM1 cells were incubated in matrigel droplets (Corning, 365234) (10,000 cells per droplet) with the addition of vehicle (H_2O) or Y27632 (20 μ M). After 16 hours images were acquired using an EVOS digital inverted fluorescence microscope and cellular

projection lengths quantified from 4 images per condition in each biological replicate using NeuriteTracer ImageJ plugin.

Network analysis

Cell connections were manually annotated from immunostained images of control (H₂O) and Y-27632 (20 μM) treated cells using ImageJ. Two cells were considered connected if their TuJ-positive projections overlapped in the images. This process yielded maps of cell association. These associations were subsequently converted into GraphML format using in-house software (convertGML, available on Github at <https://github.com/alastair-droop/associationGML>). Per node, the degree and betweenness statistics were generated from the cell association graphML files using the igraph (Csardi and Nepusz, 2006) and package in R/numerical analysis (R core team, 2018) software. Network measures were calculated using the mean of the individual node statistics for each map. A total of nine Con and ten iNet maps (representing biological replicates) were processed. GraphML files are available online at <https://doi.org/10.6084/m9.figshare.7270511.v1>.

Cell movement tracking

Cells were seeded at two distinct confluencies (>10, 75,000 cells per cm² or <50%, 200,000 cells per cm²). Following 24 hour treatment with vehicle (H₂O) or Y-27632 (20 μM), cells were monitored using the IncuCyte ZOOM system. Images were taken every 30 minutes and cellular tracking was performed on 15 distinct cells per condition from the obtained videos tracing the nuclei as the ‘point of movement’ via ImageJ software analysis (<http://rsb.info.nih.gov/ij>).

Calcium signaling and Lucifer yellow dye assays

GBM1 cells were treated with vehicle (H₂O) or Y-27632 (20 μM) for 24 hours to establish the Con and iNet cellular phenotypes. The following day, Fluo-3, AM (ThermoFisher, F23915) was added to the cells and incubated for 30 minutes in the dark at room temperature. The cells were then washed with PBS and kept in the dark for additional 30 minutes. Live cell imaging was done using the Zeiss LSM780 on a Zeiss Observer Z1 equipped with a Coherent Chameleon laser. Laser injury was performed using 100% of the Coherent Chameleon laser at 800 nm. Images were taken every 1.95 seconds. Video analysis was carried out using ImageJ software and calcium peak intensity was determined by the quantification of fluorescence intensity in 10 randomly-chosen cells before and after laser damage per imaged field. The percentage of cells in the wave was assessed by counting the number of cells that had an increase in fluorescence intensity following laser injury in relation to the total number of cells per imaged field. The Fluo-3 transmission wave angle was assessed using the ImageJ ‘angle tool’. The number of cells that transmitted the Fluo-3 signal was determined in five independent experimental repeats.

For the dye-loading via scratch assays, the Con and iNet cellular phenotypes were established in GBM1 cells using vehicle (H₂O) or Y-27632 (20 μM) respectively, cells were rinsed with PBS before the addition of 0.05% Lucifer yellow (ThermoFisher Scientific, L1177). A scratch wound was induced on the cells using a pipette tip and the dye was left on the cells for 2 minutes, allowing for its uptake. The cells were then rinsed with PBS (superfluous dye removal) and incubated with GBM media for 8 minutes. After that period life cell images were taken immediately on an A1R confocal microscope. Quantification of Lucifer Yellow transfer

was carried out by determining the number of cells containing the dye of the total number of cells in the imaged area. Five images from five independent experiments were analyzed (>500 cells per condition).

Mitochondria and Lysosome live cell staining and imaging

After establishing Con and iNet phenotypes in GBM1 cells using vehicle (H₂O) or Y-27632 (20 μM) for 24 hours, the lysosomes of the cells were stained using LysoTracker (50 nM, Thermo Fisher Scientific, L7528), and the mitochondria were stained using MitoTracker (25 nM, Thermo Fisher Scientific, M7512). LysoTracker incubation was for 2 hours, while MitoTracker incubation was for 1 hour. Subsequently, cells were fixed with 4% (w/v) PFA for 10 minutes. Images were obtained using an A1R confocal microscope. For quantification of organelles in projections, total mitochondrial volume was defined by color threshold using ImageJ (default setting, color space: HSB). Percentage of organelles in neurites were calculated by defining the area of the projections using color thresholding and determining percentage area of MitoTracker-positive signal in projections (10 images were analyzed per condition). For live cell imaging, images were taken every 30 seconds, for a total of 20 minutes, using the Zeiss LSM780 on a Zeiss Observer Z1 microscope. Mitochondrial migration was assessed using ImageJ tracking software analysis tracing 4 cells per imaging experiment utilizing 4 videos per condition.

Mitochondrial transfer assay

Mitochondria of GBM1 cells were fluorescently labelled by incubating cells for 2 hours with MitoTracker Red (25 nM) before washout and seeding in a 1:1 co-culture with GFP-expressing GBM1 cells (harbouring unlabelled mitochondria) at a total cell density of 10,000, 5,000 or 2,500 cells per cm². Con and iNet phenotypes were established using vehicle (H₂O) or Y-27632 (20 μM) for 24 hours. Cells were subsequently fixed with 4% (w/v) PFA for 15 minutes. Images were taken using an EVOS digital inverted fluorescence microscope. By defining the area of GFP-GBM1 cells by colour threshold using ImageJ (default setting, color space, HSB), the percentage area of MitoTracker positive mitochondria could be determined per cell. For analysis 5 images per condition were quantified, with >90 cells analyzed per condition. Confocal images were also taken using a Nikon A1R confocal microscope following staining with Alexa Fluor 647 Phalloidin (1:100, Invitrogen, A22287).

Radiation treatment and cellular assays comparing Con, Rev, and iNet phenotypic conditions

For cell irradiation, 20,000 cells per cm² were seeded and Con, Rev, and iNet phenotypes were established in GBM1 cells via vehicle (H₂O) exposure, Y-27632 addition (20 μM) for 24 hours, while ‘washout’ (compound withdrawal) was carried out after 16 hours of Y-27632 treatment. Subsequently, cells were irradiated with 0, 2, 8, and 20 Gy using the RadSource RS2000 irradiator

For cell behavior profiling of irradiated Con, Rev, and iNet GBM1 cells, live cell imaging was carried out immediately after radiation treatment using the IncuCyte ZOOM system. Five Con, Rev, and iNet cells were tracked for each experimental condition (0, 2, 8, and 20 Gy) for 3 days in three independent experiments, hence yielding 15 individually-traced cell behaviors per condition. An observation matrix was created by assessing each of the cells against the five following questions: 1) does the monitored cell possess elongated neurite-like

projections?, 2) is the monitored cell visually-connected to other cells via neurite-like projections?, 3) is the monitored cell motile ($>10 \mu\text{m}/\text{min}$ for Con and Rev cells and $>2.5 \mu\text{m}/\text{min}$ for iNet cells)?, 4) is the monitored cell multinucleated?, and 5) what is the observed cell fate for the monitored cell? The first four parameters were created as dichotomous variables (possible outcomes were ‘positive’ or ‘negative’). The fifth (cell fate) parameter encompassed the categories: ‘divided’ (cell division occurring during the observation period), ‘pre-division’ (no cell division occurring during the observation period), ‘cell cycle arrest’ (cells which attempted to undergo mitosis but failed in the attempt), and ‘cell death’ (indicated by cell rounding and detachment). A graphical representation of all observed cell behaviors was generated via heat map.

For the measurement of nuclear/cytoplasmic ratio, ROIs for the cytoplasmic area were defined by color thresholding using ImageJ (default setting, color space: HSB) and the percentage of area was calculated. Nuclear damage was assessed on cells based on DAPI staining: nuclei presenting with multi- or micro-nucleation segments were considered fragmented. For each radiation condition (0, 2, 8, 20 Gy), three independent experimental repeats were performed for Con, iNet and Rev cells. For each experimental repeat 10 images were analyzed per radiation condition and treatment.

For the cell viability assay, GBM1 cells were seeded at densities of 10,000 cells per well in white 96-well plates (Greiner bio-one, 655083), and subsequently, Con, Rev, and iNet phenotypes were established (with the aforementioned treatments) and cells were subject to (0, 2, 8, and 20 Gy) radiation treatments. After 5 days, the CellTiter-Glo assay (Promega, G7572) was used, and following equilibration of reagents and cells to room temperature, 100 μL of CellTiter-Glo reagent was added to each and incubation was for 10 minutes in the dark. The luminescence signal was measured using the Mithras LB 940 plate reader.

Extracellular flux-based metabolic assessment of Con, Rev, and iNet GBM1 cells was carried out five days after (0 and 20 Gy) radiation treatments using the Seahorse XF extracellular flux analyzer and protocols described in (Pike Winer and Wu, 2014). Cells were trypsinized and seeded into the manufacturer's microplates at a density of 30,000 cells per well. Before analysis, the medium was replaced with XF base media (Seahorse Bioscience, 102353-100) and transferred to a 37°C non-CO₂ humidified incubator. For the “Mito stress test”, XF base medium was supplemented with glucose (25 mM, Sigma, G8769), sodium pyruvate (0.5 mM, Sigma, S8636) and L-glutamine (2 mM, Gibco, 35050-061). The final medium was adjusted to pH 7.4 and filtered using a 0.2 μM filter. Oligomycin (1 μM), FCCP (0.5 μM), antimycin and rotenone (0.5 μM) were injected according to the “Mito Stress Test” (Seahorse Bioscience, 101848- 400) protocol and results were analyzed using ‘Mito Stress Test’ kit protocols.

RNA-seq transcriptional profiling

RNA sequencing of GBM1 cells was performed under Rev and iNet conditions. Following a 24-hour treatment with Y-27632 and 8 hour washout, cells were subjected to 0 and 20 Gy. Five days following irradiation, total RNA was isolated from three biological replicates of 0 and 20 Gy/Rev and iNet conditions using RNeasy Mini kits following the manufacturer’s instructions (Qiagen; 74106). The integrity and concentration of RNA were determined using Qubit® RNA Assay Kit in Qubit® 2.0 Fluorometer (Life Technologies, CA, USA). A total amount of 3 μg RNA was used per condition for RNA sample preparation. Sequencing libraries were generated using NEBNext® Ultra™ RNA Library Prep Kit for Illumina® (NEB, USA) following manufacturer’s recommendations and index codes were added to attribute sequences

to each sample. The clustering of the index-coded samples was performed on a cBot Cluster Generation System using HiSeq PE Cluster Kit cBot-HS (Illumina) according to the manufacturer's instructions. After cluster generation, the library preparations were sequenced on an Illumina HiSeq platform and 125 bp/150 bp paired-end reads were generated. Sequenced reads were quality-processed, aligned and differential expression analysis performed as described in (Conway et al., 2015), with the exception that the alignment was to the hg38 human reference genome using STAR aligner (v2.2.1) (Dobin et al., 2013). Briefly, reads were trimmed to retain quality and adapters removed, aligned to the human genome and quantified prior to paired sample differential gene expression analysis across groups.

Statistical analysis

Statistical details are provided in the figure legends. Data were analyzed by a two-sided paired Student's t-test, One-way/Two-way ANOVA (Microsoft Office Professional Plus 2013 package and/or GraphPad Prism software version 7.05), or the Mann-Whitney U test (assessing data from several dynamic cellular measurements). Heatmap and volcano plot visualization was done in Excel (Microsoft Office Professional Plus 2013 package). Network degree and betweenness statistics were generated using the igraph (Csardi and Nepusz 2006) and R/numerical analysis (R core team 2018) software.

Data availability

Network analysis (GraphML) files are available online at <https://doi.org/10.6084/m9.figshare.7270511.v1> and the software at <https://github.com/alastair-droop/associationGML>.

The RNA-seq transcriptional profiling data has been deposited into The European Nucleotide Archive under accession number PRJEB26811.

Acknowledgements

We thank Mihaela Lorger and Anestis Tsakiridis for critical advice.

Competing interest

The authors declare no conflict of interest.

Author contributions

Conceptualization: B. d.S., E.S.P., G.M., H.W; Experiments/analysis: B.d.S., B.K.I., E.S.P., A.D., H.B.S.G., C.W., J.W., M.S., S.J.A., H.W.; Methodology: A.D., L.F.S., J.M., P.J.O.T; Writing - original draft: B.d.S., H.W; Writing - review and editing: B.d.S., B.K.I., R.K.M., S.C.S., P.J.O.T, S.J.A., G.M., H.W. Supervision: P.J.O.T, S.J.A., G.M., H.W.

Funding

We acknowledge support from the Brain Tumour Research and Support across Yorkshire charity (including 'The Ian Meek PhD studentship) and the Medical Research Council (MR/J001171/1). R.K.M. acknowledges support from Candlelighters and A.D. acknowledges support from the UKRI Rutherford fellowship (MR/S00386X/1).

REFERENCES

- Ahmed, Z., Douglas, M. R., John, G., Berry, M. and Logan, A.** (2013). AMIGO3 is an NgR1/p75 co-receptor signalling axon growth inhibition in the acute phase of adult central nervous system injury. *PLoS ONE* **8**, e61878.
- Azzam, E. I., Jay-Gerin, J.-P. and Pain, D.** (2012). Ionizing radiation-induced metabolic oxidative stress and prolonged cell injury. *Cancer Lett.* **327**, 48–60.
- Bao, S., Wu, Q., McLendon, R. E., Hao, Y., Shi, Q., Hjelmeland, A. B., Dewhirst, M. W., Bigner, D. D. and Rich, J. N.** (2006). Glioma stem cells promote radioresistance by preferential activation of the DNA damage response. *Nature* **444**, 756–760.
- Caino, M. C., Chae, Y. C., Vaira, V., Ferrero, S., Nosotti, M., Martin, N. M., Weeraratna, A., O’Connell, M., Jernigan, D., Fatatis, A., et al.** (2013). Metabolic stress regulates cytoskeletal dynamics and metastasis of cancer cells. *J. Clin. Invest.* **123**, 2907–2920.
- Caino, M. C., Seo, J. H., Aguinaldo, A., Wait, E., Bryant, K. G., Kossenkov, A. V., Hayden, J. E., Vaira, V., Morotti, A., Ferrero, S., et al.** (2016). A neuronal network of mitochondrial dynamics regulates metastasis. *Nat. Commun.* **7**, 13730.
- Conway, C., Graham, J. L., Chengot, P., Daly, C., Chalkley, R., Ross, L., Droop, A., Rabbitts, P. and Stead, L. F.** (2015). Elucidating drivers of oral epithelial dysplasia formation and malignant transformation to cancer using RNAseq. *Oncotarget* **6**, 40186–40201.
- Csardi, G. and Nepusz, T.** (2006). The igraph software package for complex network research. *Interjournal Complex Systems*, 1695.
- Davis, M. E.** (2016). Glioblastoma: overview of disease and treatment. *Clin. J. Oncol. Nurs.* **20**, S2-8.
- da Silva, B., Mathew, R. K., Polson, E. S., Williams, J. and Wurdak, H.** (2018). Spontaneous Glioblastoma Spheroid Infiltration of Early-Stage Cerebral Organoids Models Brain Tumor Invasion. *SLAS Discov.* **23**, 2472555218764623.
- Dergham, P., Ellezam, B., Essagian, C., Avedissian, H., Lubell, W. D. and McKerracher, L.** (2002). Rho signaling pathway targeted to promote spinal cord repair. *J. Neurosci.* **22**, 6570–6577.
- Dobin, A., Davis, C. A., Schlesinger, F., Drenkow, J., Zaleski, C., Jha, S., Batut, P., Chaisson, M. and Gingeras, T. R.** (2013). STAR: ultrafast universal RNA-seq aligner. *Bioinformatics* **29**, 15–21.
- Doe, C., Bentley, R., Behm, D. J., Lafferty, R., Stavenger, R., Jung, D., Bamford, M., Panchal, T., Grygielko, E., Wright, L. L., et al.** (2007). Novel Rho kinase inhibitors with anti-inflammatory and vasodilatory activities. *J. Pharmacol. Exp. Ther.* **320**, 89–98.
- Drubin, D. G., Feinstein, S. C., Shooter, E. M. and Kirschner, M. W.** (1985). Nerve growth factor-induced neurite outgrowth in PC12 cells involves the coordinate induction of microtubule assembly and assembly-promoting factors. *J. Cell Biol.* **101**, 1799–1807.

- el-Fouly, M. H., Trosko, J. E. and Chang, C. C.** (1987). Scrape-loading and dye transfer. A rapid and simple technique to study gap junctional intercellular communication. *Exp. Cell Res.* **168**, 422–430.
- El Hallani, S., Boisselier, B., Peglion, F., Rousseau, A., Colin, C., Idbaih, A., Marie, Y., Mokhtari, K., Thomas, J.-L., Eichmann, A., et al.** (2010). A new alternative mechanism in glioblastoma vascularization: tubular vasculogenic mimicry. *Brain* **133**, 973–982.
- Fournier, A. E., Takizawa, B. T. and Strittmatter, S. M.** (2003). Rho kinase inhibition enhances axonal regeneration in the injured CNS. *J. Neurosci.* **23**, 1416–1423.
- Francescone, R. A., Faibish, M. and Shao, R.** (2011). A Matrigel-based tube formation assay to assess the vasculogenic activity of tumor cells. *J. Vis. Exp.* **7**, pii: 3040. doi: 10.3791/3040.
- Fujita, Y. and Yamashita, T.** (2014). Axon growth inhibition by RhoA/ROCK in the central nervous system. *Front. Neurosci.* **8**, 338.
- Garton, A. J., Castaldo, L. and Pachter, J. A.** (2008). Quantitative high-throughput cell-based assays for inhibitors of ROCK kinases. In *Small gtpases in disease, part B*, pp. 491–500. Elsevier.
- Grossman, S. A. and Batara, J. F.** (2004). Current management of glioblastoma multiforme. *Semin. Oncol.* **31**, 635–644.
- Huang, D. W., Sherman, B. T. and Lempicki, R. A.** (2009a). Systematic and integrative analysis of large gene lists using DAVID bioinformatics resources. *Nat. Protoc.* **4**, 44–57.
- Huang, D. W., Sherman, B. T. and Lempicki, R. A.** (2009b). Bioinformatics enrichment tools: paths toward the comprehensive functional analysis of large gene lists. *Nucleic Acids Res.* **37**, 1–13.
- Ikenoya, M., Hidaka, H., Hosoya, T., Suzuki, M., Yamamoto, N. and Sasaki, Y.** (2002). Inhibition of rho-kinase-induced myristoylated alanine-rich C kinase substrate (MARCKS) phosphorylation in human neuronal cells by H-1152, a novel and specific Rho-kinase inhibitor. *J. Neurochem.* **81**, 9–16.
- Jackson, M. D. B., Duran-Nebreda, S. and Bassel, G. W.** (2017). Network-based approaches to quantify multicellular development. *J. R. Soc. Interface* **14**, pii: 20170484. doi: 10.1098/rsif.2017.0484.
- Jia, X.-F., Ye, F., Wang, Y.-B. and Feng, D.-X.** (2016). ROCK inhibition enhances neurite outgrowth in neural stem cells by upregulating YAP expression in vitro. *Neural Regen. Res.* **11**, 983–987.
- King, H. O., Brend, T., Payne, H. L., Wright, A., Ward, T. A., Patel, K., Egnuni, T., Stead, L. F., Patel, A., Wurdak, H., et al.** (2017). RAD51 is a selective DNA repair target to radiosensitize glioma stem cells. *Stem Cell Reports* **8**, 125–139.
- Kranenburg, O., Poland, M., van Horck, F. P., Drechsel, D., Hall, A. and Moolenaar, W. H.** (1999). Activation of RhoA by lysophosphatidic acid and Galpha12/13 subunits in neuronal cells: induction of neurite retraction. *Mol. Biol. Cell* **10**, 1851–1857.

- Kuo, L. J. and Yang, L.-X.** (2008). Gamma-H2AX - a novel biomarker for DNA double-strand breaks. *In Vivo* **22**, 305–309.
- Maekawa, M., Ishizaki, T., Boku, S., Watanabe, N., Fujita, A., Iwamatsu, A., Obinata, T., Ohashi, K., Mizuno, K. and Narumiya, S.** (1999). Signaling from Rho to the actin cytoskeleton through protein kinases ROCK and LIM-kinase. *Science* **285**, 895–898.
- Minta, A., Kao, J. P. and Tsien, R. Y.** (1989). Fluorescent indicators for cytosolic calcium based on rhodamine and fluorescein chromophores. *J. Biol. Chem.* **264**, 8171–8178.
- Newman, M. E. J.** (2006). Modularity and community structure in networks. *Proc Natl Acad Sci USA* **103**, 8577–8582.
- Ohashi, K., Nagata, K., Maekawa, M., Ishizaki, T., Narumiya, S. and Mizuno, K.** (2000). Rho-associated kinase ROCK activates LIM-kinase 1 by phosphorylation at threonine 508 within the activation loop. *J. Biol. Chem.* **275**, 3577–3582.
- Osswald, M., Jung, E., Sahm, F., Solecki, G., Venkataramani, V., Blaes, J., Weil, S., Horstmann, H., Wiestler, B., Syed, M., et al.** (2015). Brain tumour cells interconnect to a functional and resistant network. *Nature* **528**, 93–98.
- Ostrom, Q. T., Bauchet, L., Davis, F. G., Deltour, I., Fisher, J. L., Langer, C. E., Pekmezci, M., Schwartzbaum, J. A., Turner, M. C., Walsh, K. M., et al.** (2014). The epidemiology of glioma in adults: a “state of the science” review. *Neuro Oncol.* **16**, 896–913.
- Osuka, S. and Van Meir, E. G.** (2017). Overcoming therapeutic resistance in glioblastoma: the way forward. *J. Clin. Invest.* **127**, 415–426.
- Pike Winer, L. S. and Wu, M.** (2014). Rapid analysis of glycolytic and oxidative substrate flux of cancer cells in a microplate. *PLoS ONE* **9**, e109916.
- Polson, E. S., Kuchler, V. B., Abbosh, C., Ross, E. M., Mathew, R. K., Beard, H. A., da Silva, B., Holding, A. N., Ballereau, S., Chuntharpursat-Bon, E., et al.** (2018). KHS101 disrupts energy metabolism in human glioblastoma cells and reduces tumor growth in mice. *Sci. Transl. Med.* **10**(454). pii: eaar2718. doi: 10.1126/scitranslmed.aa2718.
- Pool, M., Thiemann, J., Bar-Or, A. and Fournier, A. E.** (2008). NeuriteTracer: a novel ImageJ plugin for automated quantification of neurite outgrowth. *J. Neurosci. Methods* **168**, 134–139.
- Rath, N. and Olson, M. F.** (2012). Rho-associated kinases in tumorigenesis: re-considering ROCK inhibition for cancer therapy. *EMBO Rep.* **13**, 900–908.
- Ross-Macdonald, P., de Silva, H., Guo, Q., Xiao, H., Hung, C.-Y., Penhallow, B., Markwalder, J., He, L., Attar, R. M., Lin, T., et al.** (2008). Identification of a nonkinase target mediating cytotoxicity of novel kinase inhibitors. *Mol. Cancer Ther.* **7**, 3490–3498.
- R core team** (2018). *R: a language and environment for statistical computing*. Vienna Austria: R Foundation for Statistical Computing.
- Salhia, B., Rutten, F., Nakada, M., Beaudry, C., Berens, M., Kwan, A. and Rutka, J. T.** (2005). Inhibition of Rho-kinase affects astrocytoma morphology, motility, and invasion through activation of Rac1. *Cancer Res.* **65**, 8792–8800.

- Sanz-Moreno, V., Gaggioli, C., Yeo, M., Albregues, J., Wallberg, F., Viros, A., Hooper, S., Mitter, R., F eral, C. C., Cook, M., et al.** (2011). ROCK and JAK1 signaling cooperate to control actomyosin contractility in tumor cells and stroma. *Cancer Cell* **20**, 229–245.
- Straight, A. F., Cheung, A., Limouze, J., Chen, I., Westwood, N. J., Sellers, J. R. and Mitchison, T. J.** (2003). Dissecting temporal and spatial control of cytokinesis with a myosin II Inhibitor. *Science* **299**, 1743–1747.
- Subramanian, A., Tamayo, P., Mootha, V. K., Mukherjee, S., Ebert, B. L., Gillette, M. A., Paulovich, A., Pomeroy, S. L., Golub, T. R., Lander, E. S., et al.** (2005). Gene set enrichment analysis: a knowledge-based approach for interpreting genome-wide expression profiles. *Proc Natl Acad Sci USA* **102**, 15545–15550.
- Tilson, S. G., Haley, E. M., Triantafillu, U. L., Dozier, D. A., Langford, C. P., Gillespie, G. Y. and Kim, Y.** (2015). ROCK Inhibition Facilitates In Vitro Expansion of Glioblastoma Stem-Like Cells. *PLoS ONE* **10**, e0132823.
- Torrallba, D., Baixauli, F. and S anchez-Madrid, F.** (2016). Mitochondria know no boundaries: mechanisms and functions of intercellular mitochondrial transfer. *Front. Cell Dev. Biol.* **4**, 107.
- Wharton, S. B., Chan, K. K. and Whittle, I. R.** (2002). Microtubule-associated protein 2 (MAP-2) is expressed in low and high grade diffuse astrocytomas. *J. Clin. Neurosci.* **9**, 165–169.
- Wurdak, H.** (2012). Exploring the cancer stem cell phenotype with high-throughput screening applications. *Future Med. Chem.* **4**, 1229–1241.
- Wurdak, H., Zhu, S., Romero, A., Lorgner, M., Watson, J., Chiang, C.-Y., Zhang, J., Natu, V. S., Lairson, L. L., Walker, J. R., et al.** (2010). An RNAi screen identifies TRRAP as a regulator of brain tumor-initiating cell differentiation. *Cell Stem Cell* **6**, 37–47.
- Zohrabian, V. M., Forzani, B., Chau, Z., Murali, R. and Jhanwar-Uniyal, M.** (2009). Rho/ROCK and MAPK signaling pathways are involved in glioblastoma cell migration and proliferation. *Anticancer Res.* **29**, 119–123.

Figures

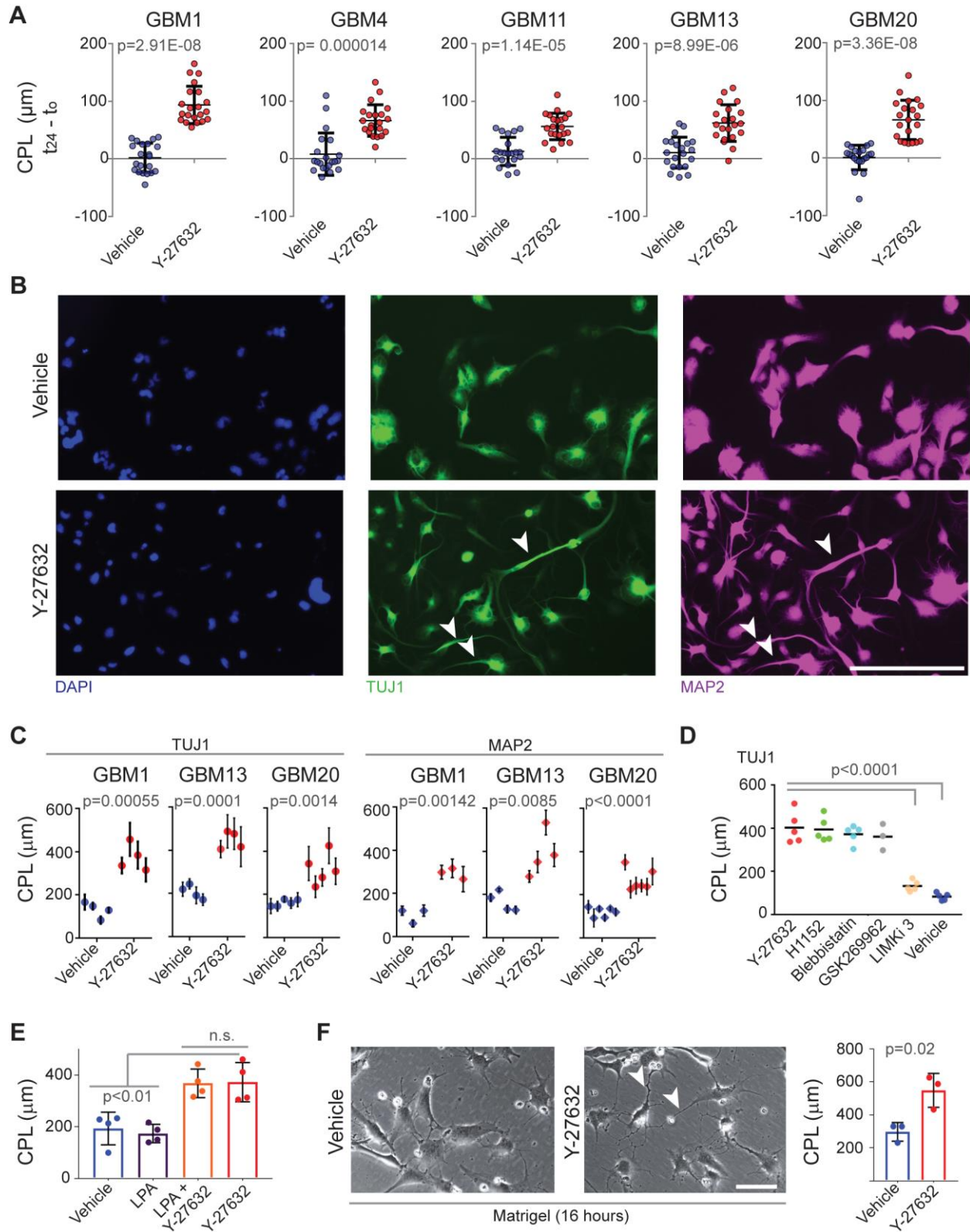


Figure 1. Chemical ROCK inhibition elongates cellular projection length (CPL) in patient-derived GBM cell models. (A) Dots are changes in CPL (μm ; $t_{24} - t_0$ values) of 21 individually-traced cells per indicated GBM cell line treated with vehicle (H_2O) or Y-27632 ($20 \mu\text{M}$). Plots indicate the median with 95% confidence intervals. (B) Immunocytochemistry images of projections (indicated by arrowheads) in vehicle (H_2O)- or Y-27632 ($20 \mu\text{M}$)-treated GBM1 cells stained for MAP2 and TuJ1. Scale bar, $200 \mu\text{m}$. (C) Dots are mean TuJ1- and MAP2-positive CPL values of independent experiments (\pm standard deviation) 24 hours after vehicle (H_2O) or Y-27632 ($20 \mu\text{M}$) treatments using indicated cell models (~ 200 cells analyzed per treatment). (D) Data are mean CPL values of independent experiments (black lines: median) in presence of vehicle (H_2O) or the indicated small molecule inhibitors. (E) Dots are mean CPL values of independent experiments (bars: mean \pm standard deviation) following 24 hour pre-treatment with vehicle (H_2O) or Y-27632 ($20 \mu\text{M}$), and subsequent 8-hour treatment with LPA ($1 \mu\text{M}$), or vehicle, or LPA ($1 \mu\text{M}$)/Y-27632 ($20 \mu\text{M}$), or Y-27632 ($20 \mu\text{M}$); ~ 200 cells analyzed per treatment). (F) Left, representative images of GBM1 cells following a 16-hour period in matrigel with vehicle (H_2O) or Y-27632 ($20 \mu\text{M}$) treatments. Arrowheads depict neurite-like outgrowth. Scale bar, $20 \mu\text{m}$. Right, data are mean CPL values of independent experiments (bars: mean \pm standard deviation; >260 cells analyzed per indicated treatment). The p-values were determined by Mann-Whitney U test (two-tailed; A), Student's t-test (2-tailed, equal variance; C), and One-way ANOVA (D, E, F).

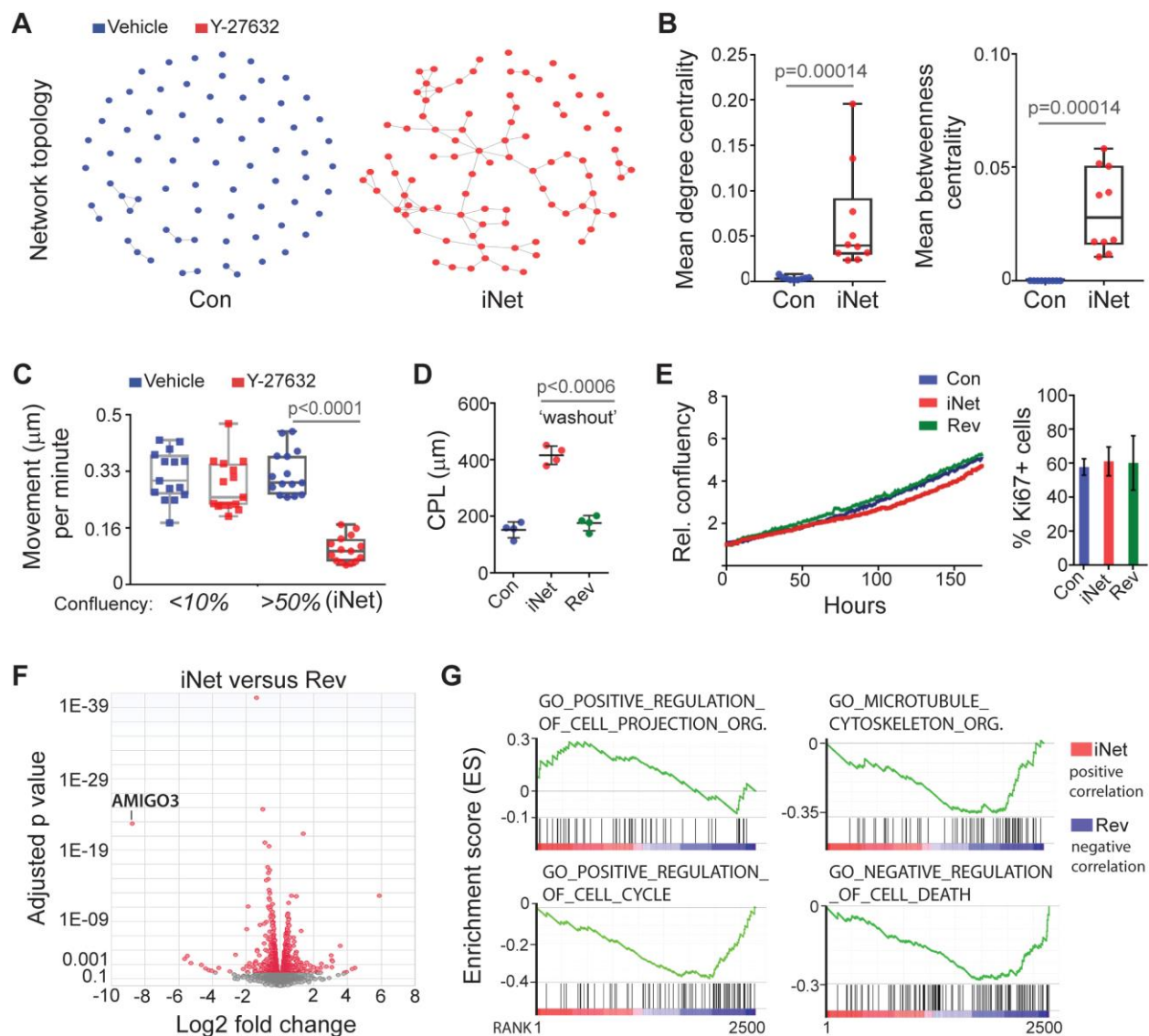


Figure 2. Chemically-induced *de novo* network formation in GBM cells. (A) Representative topologies of vehicle control (Con; left) or Y-27632-induced GBM1 cell networks (iNet, right). (B) Con versus iNet network modal degree (left) and betweenness (right) values of independent experiments. (C) Data are individual GBM1 cell movement distances under indicated confluency and treatment. Plots indicate the median with 95% confidence intervals. (D) Data are mean CPL values of independent experiments (\pm standard deviation) using Con, iNet, or Rev (Y-27632 ‘washout’) conditions (\sim 200 cells analyzed per condition). (E) Left, real-time assessment of GBM1 Con, iNet, or Rev cell confluency (fold change normalized to t_0). One out of three independent experiments is shown. Right, mean percentages of Ki67-expressing Con, iNet, or Rev cells (3 independent experiments \pm standard deviation; >1500 cells analyzed per condition). (F) Volcano plot comparing transcriptional RNA-seq profiles of genes in iNet versus Rev conditions in GBM1 cells passing a threshold false discovery rate (FDR) <5% (indicated by red color) based on three independent experiments. The log₂ fold change expression is shown and

negative values indicate genes showing a decrease in expression in iNet compared to Rev conditions. (G) GSEA plots of ranked gene expression (FDR <5%) comparing transcriptional iNet and Rev profiles and their positive (red) and negative (blue) correlations for the indicated gene sets. Enrichment scores are shown as green lines, and the horizontal black bars indicate the position of the associated genes for each enrichment set. The p-values were determined by the Mann-Whitney U test (one-tailed; B), and One-way ANOVA (C, D). Plots (B,C) indicate the median with 95% confidence intervals.

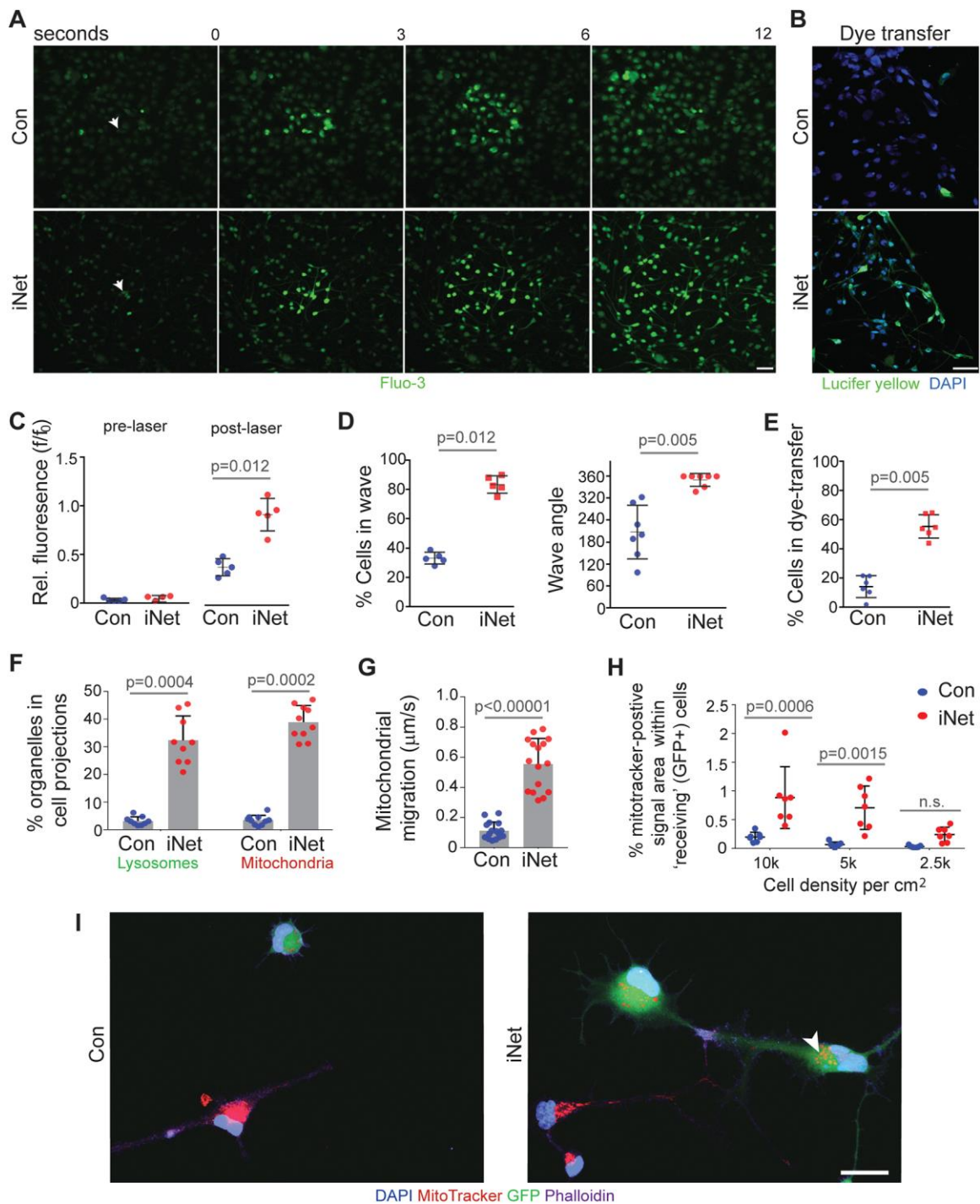


Figure 3. The iNet phenotype promotes multicellular cooperation. (A) Still frame images of intracellular Fluo-3 transmission upon laser irradiation of a single Con or iNet GBM1 cell (indicated by arrowheads). Scale bar, 30 μm . (B) Microscopic false color image of Lucifer yellow dye transfer using scrape loading technique in Con or iNet cells. Scale bar, 50 μm . (C) Data are means of Fluo-3 signal intensities of independent (pre- and post-laser) experiments (\pm

standard deviation) using Con or iNet conditions. (D) Left, mean percentages of independent (post-laser) experiments assessing total Con or iNet cells transmitting the Fluo-3 wave. Right, mean wave transmission angle values per imaged field in independent experiments. (E) Mean percentages of Lucifer yellow-transferring cells (\pm standard deviation) of independent experiments (>500 cells were analyzed per Con or iNet condition). (F) Dots are mean percentages of independent experiments assessing lysosomal and mitochondrial signals within Co or iNet cell projections (bars: mean + standard deviation). (G) Dots represent migration distances of 4 individually-traced mitochondria per 4 independent imaging experiments in Con or iNet cells (bars: mean + standard deviation). (H) Values are mean percentages of independent experiments (\pm standard deviation) assessing MitoTracker-positive signals within GFP-expressing Con or iNet 'recipient' cells per indicated cell seeding density (>90 cells analyzed per condition). (I) Confocal microscopy images of 'donor' (GBM1 MitoTracker-positive) and 'recipient' (GBM1 GFP-positive) Con or iNet cells with the indicated stainings. Arrowhead depicts transferred mitochondria. Scale bar, 20 μ m. The p-values were determined by the Mann-Whitney U Test (one-tailed) except for (H) where Two-way ANOVA was used.

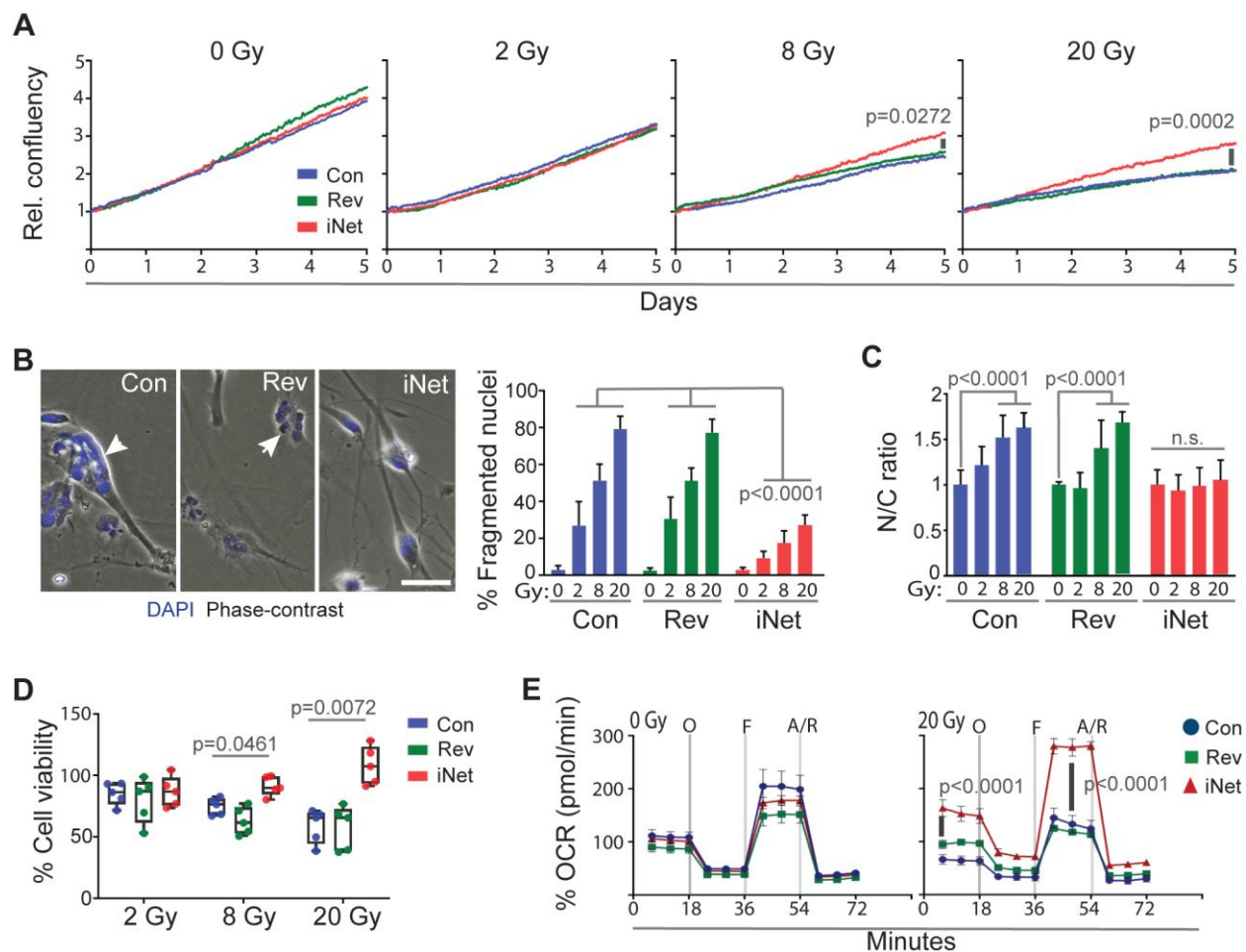


Figure 4. iNet increases cellular radiation resistance. (A) Real-time assessment of GBM1 cell confluency (fold change normalized to t_0) in Con, iNet, or Rev GBM1 cells upon radiation with the indicated doses. One out of three biological replicates is shown. (B) Left, images of fragmented nuclei (indicated by arrowheads) in Con, Rev, or iNet GBM1 cells 5 days after irradiation. Scale bar, 20 μm . Right, bars are mean percentages of fragmented nuclei of three independent experiments (+ standard deviation) using the indicated radiation doses (≥ 500 cells analyzed per condition). (C) Bars depicts the means of GBM1 nuclear/cytoplasmic (N/C) ratios of three independent experiments (+ standard deviation) in Con, Rev, or iNet cells 5 days after irradiation with the indicated doses. (D) Data are means of independent cell viability experiments in Con, Rev, or iNet cells 5 days after irradiation with the indicated doses, relative to the non-irradiated control. Plots indicate the median with 95% confidence intervals. (E) Mitochondrial bioenergetic (extracellular flux) analysis of GBM1 cells 5 days after 20 Gy irradiation. OCR, oxygen consumption rate; O, Oligomycin; F, FCCP; A/R, Antimycin/Rotenone. Data are the means of three biological replicates (\pm standard deviation). The p-values were determined by One-way ANOVA (A, B, E), and Two-way ANOVA (C, D) tests.

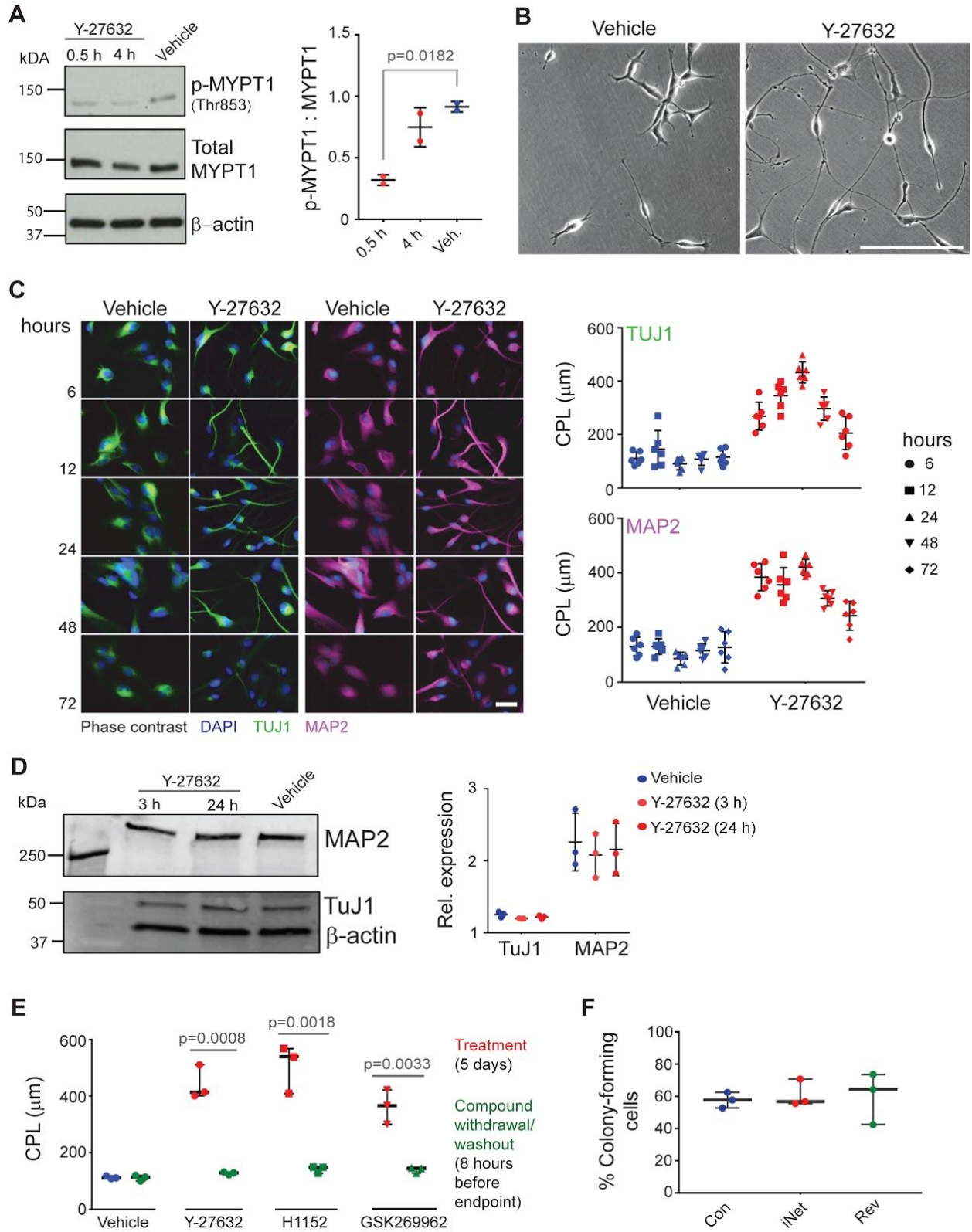
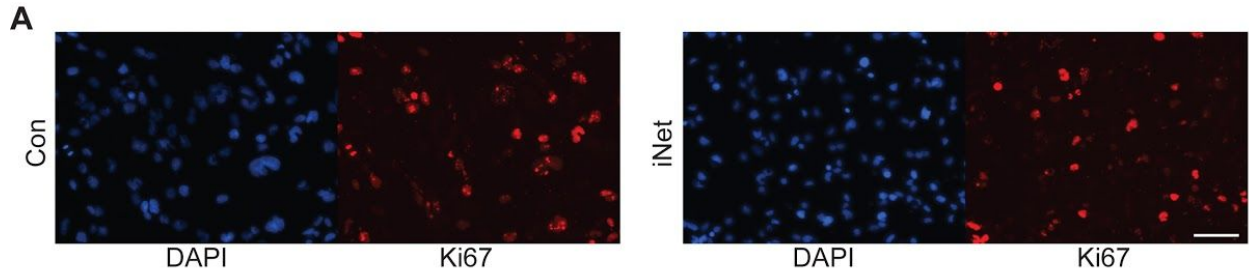


Fig. S1. Chemical ROCK inhibition reversibly induces neurite-like outgrowth in GBM1 cells. (A) Left, immunoblot detecting phosphorylated and total MYPT1 protein in LPA-stimulated GBM1

cells (1 μM , over night) followed by Y-27632 (20 μM) or vehicle (H_2O) treatments for the indicated time points. Right, the ratio of phosphorylated MYPT1 (p-MYPT1) and total MYPT1 (as determined by gel densitometry). Dots represent independent repeats. (B) Representative phase contrast images of GBM1 cells following treatment with Y-27632 (20 μM) or vehicle (H_2O) for 24 hours. Scale bar, 200 μm (C) Time course of Y-27632 (20 μM)-induced neurite-like projection outgrowth in GBM1 cells. Left, immunofluorescence images of cells and projections stained for TUJ1 and MAP2 over the indicated time course. Scale bar, 20 μm . Right, symbols are mean CPL values of three technical repeats obtained from two independent experiments (\pm standard deviation) comparing vehicle and Y-27632 (20 μM) treatments at the indicated time points (\sim 200 cells analyzed per treatment experiment). (D) Left, immunoblot showing total protein levels of MAP2 and TuJ1 in GBM1 cells following the indicated treatments with Y-27632 (20 μM) or vehicle (H_2O). Right, the beta-actin control was used to normalize data yielding relative MAP2 and TuJ1 expression levels. Three independent experiments (dots, \pm standard deviation) are shown. (E) Data are means of independent experiments (\pm standard deviation) showing TuJ1-positive CPL values in GBM1 cells after 5-day treatments with vehicle (H_2O), Y-27632 (20 μM), H1152 (10 μM), and GSK269962 (5 μM) as compared with compound withdrawal (washout) 8 hours before the experimental endpoint. (F) Clonal growth capacity of individual GBM1 cells (%) in the Con, iNet, and Rev phenotypic conditions. Data are means from three independent experiments (\pm standard deviation, horizontal black line: average). The p-values were determined by a two-sided Student's T-test test (equal variance).



B

Category	Term	RT	Genes	Count	%	P-Value	Benjamini
KEGG_PATHWAY	Focal adhesion	RT		44	2.2	2.4E-5	6.6E-3
KEGG_PATHWAY	Hippo signaling pathway	RT		35	1.7	3.4E-5	4.7E-3
KEGG_PATHWAY	Axon guidance	RT		31	1.5	3.7E-5	3.5E-3
KEGG_PATHWAY	p53 signaling pathway	RT		20	1.0	7.5E-5	5.3E-3
KEGG_PATHWAY	Cell cycle	RT		29	1.4	1.6E-4	8.6E-3
KEGG_PATHWAY	Rap1 signaling pathway	RT		42	2.1	1.8E-4	8.2E-3
KEGG_PATHWAY	Pathways in cancer	RT		67	3.3	2.7E-4	1.1E-2
KEGG_PATHWAY	Cell adhesion molecules (CAMs)	RT		31	1.5	3.2E-4	1.1E-2
KEGG_PATHWAY	Lysosome	RT		27	1.3	6.0E-4	1.8E-2
KEGG_PATHWAY	FoxO signaling pathway	RT		29	1.4	6.0E-4	1.7E-2
KEGG_PATHWAY	TGF-beta signaling pathway	RT		21	1.0	6.4E-4	1.6E-2
KEGG_PATHWAY	HIF-1 signaling pathway	RT		23	1.1	8.3E-4	1.9E-2
KEGG_PATHWAY	HTLV-I infection	RT		46	2.3	9.7E-4	2.1E-2
KEGG_PATHWAY	Proteoglycans in cancer	RT		38	1.9	1.0E-3	2.1E-2
KEGG_PATHWAY	Central carbon metabolism in cancer	RT		16	0.8	3.5E-3	6.3E-2

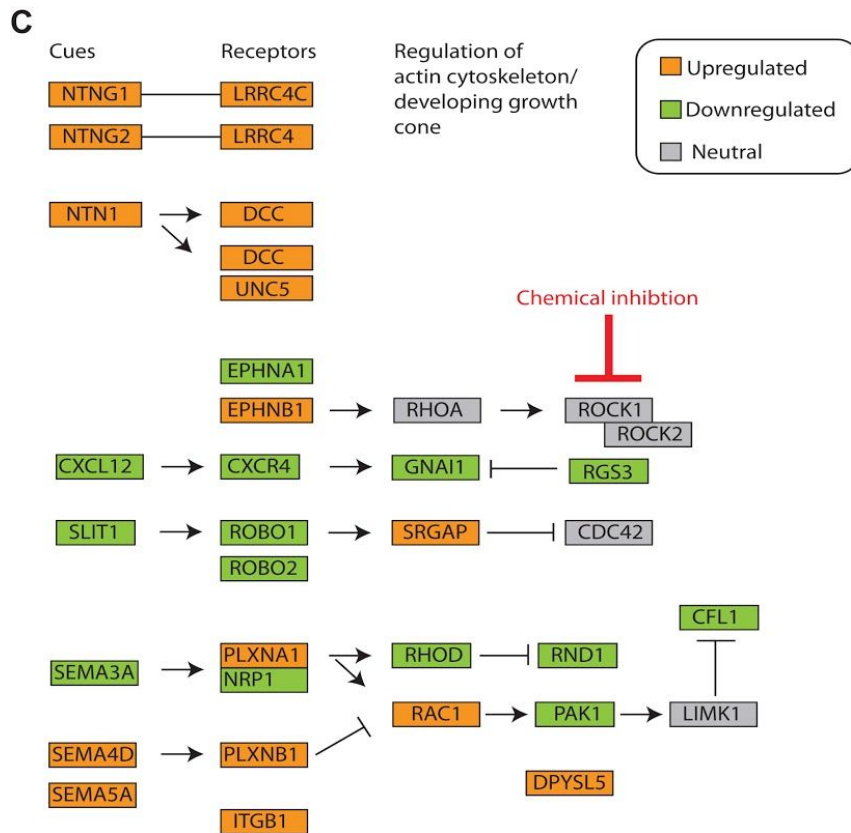


Fig. S2. GBM cells sustain proliferation and upregulate axon guidance pathways in iNet versus control conditions. (A) Representative immunofluorescence images of Ki67 staining in GBM1 cells following treatment with Y-27632 (20 μ M) or vehicle (H_2O) for 24 hours. Scale bar, 50 μ m. (B) DAVID functional annotation suggests iNet-specific enrichment of axonal guidance- and actin cytoskeleton-regulating genes. A list of kyoto encyclopedia of genes and genomes (KEGG; (Kanehisa and Goto 2000)) pathways that were differentially regulated ($p < 0.005$) in the iNet compared with the Rev (RNA expression) profile of GBM1 cells is provided. (C) Scheme displaying the 31 genes of the KEGG axon guidance pathway that were significantly enriched in the iNet profile.

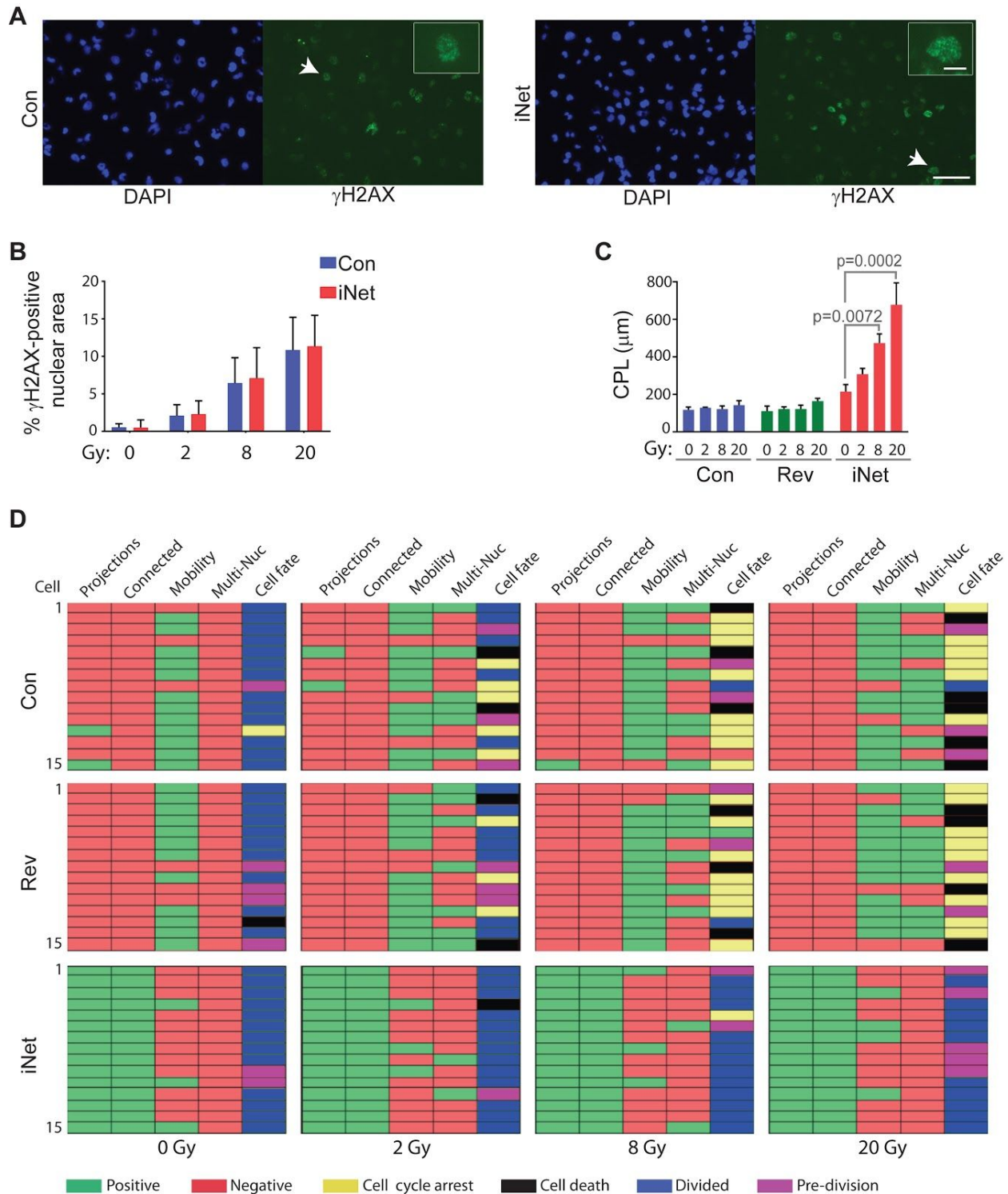


Fig. S3. GBM1 iNET cells exhibit increased cell projection outgrowth and survival upon radiation treatment. (A) Representative immunofluorescence images of DAPI (blue) and γ H2AX (green) staining following 8 Gy radiation treatment in Con or iNet conditions. Arrowhead depicts damaged nuclei and punctate γ H2AX foci shown in (higher zoom) inlay panels. Scale bars, 50

μm and 5 μm (inlay). (B) Quantification of $\gamma\text{-H2AX}$ -stained nuclear area in GBM1 cells under Con and iNet phenotypic conditions 2 hours after 0, 2, 8, and 20 Gy radiation treatments. Data are means of three independent experiments (bars: mean + standard deviation) using 5 different imaging fields (>200 cells) per repeat. (C) Data are mean CPL values of three independent experiments (bars: mean + standard deviation) per Con, iNet, and Rev conditions 5 days after 0, 2, 8, and 20 Gy radiation treatments. The p-values were determined by 1-Way ANOVA. (D) Cell behaviour analysis depicting the presence (green bars) or absence (red bars) of the indicated cell morphologies (elongated projections, connections with other cells, cell mobility, multi-nucleation), and cell fates (color code: cell cycle arrest, yellow; cell division, blue; pre-division cell state, purple; cell death, black) as assessed by real time imaging for 15 cells randomly-chosen from Con, Rev, and iNet GBM1 cultures treated with the indicated radiation doses. Data indicate that most iNet cells were connected via cell projections and displayed a low motility phenotype. Taking the total of 45 analyzed cells in all radiation treatments into account, both cell cycle arrest and cell death were reduced by $\sim 90\%$, and multinucleation by $\sim 80\%$ in iNet cells compared to their Con and Rev counterparts. Thirty-five irradiated iNet cells underwent mitosis, whereas only 7 and 8 Con and Rev cells divided, respectively.

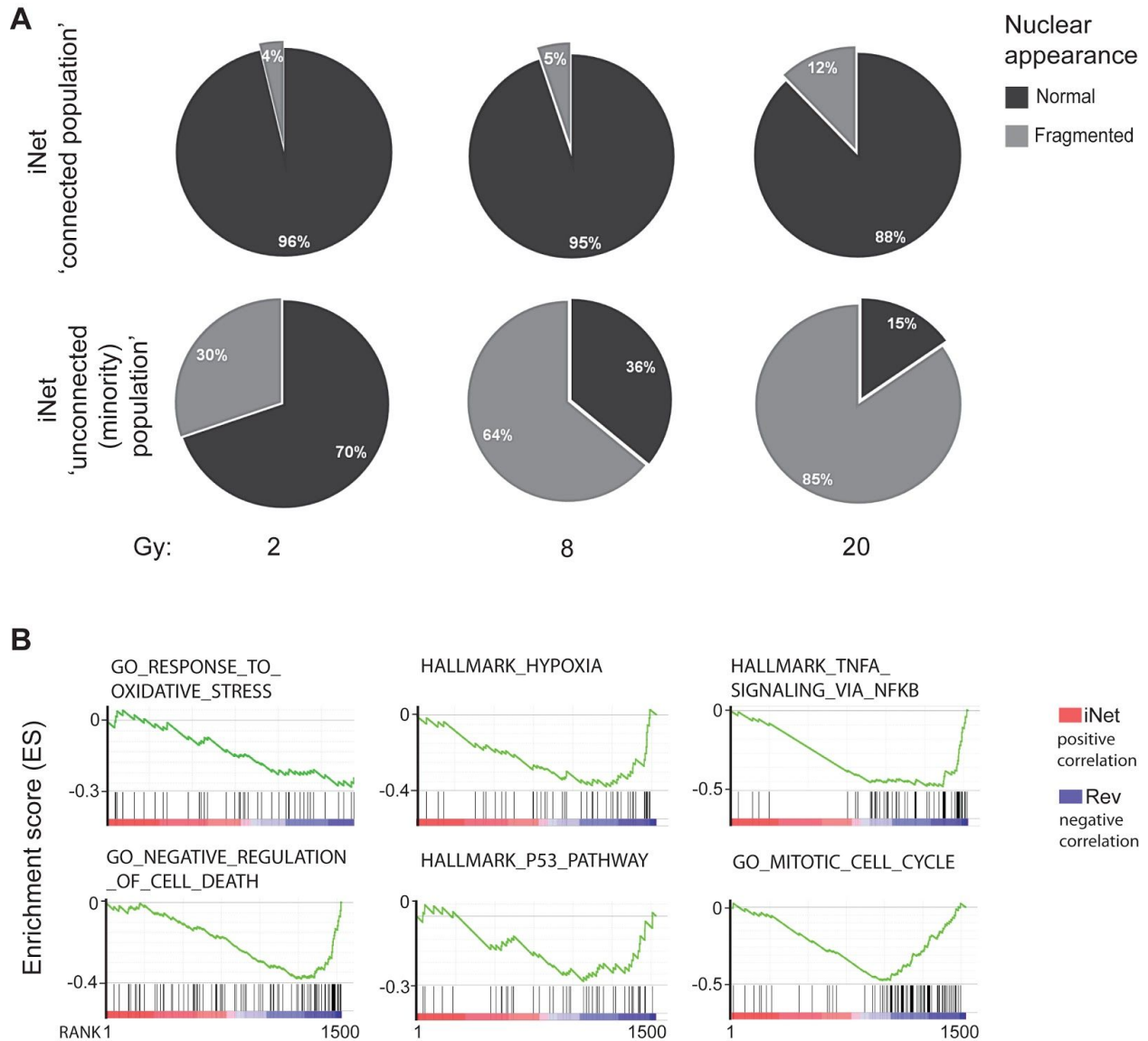
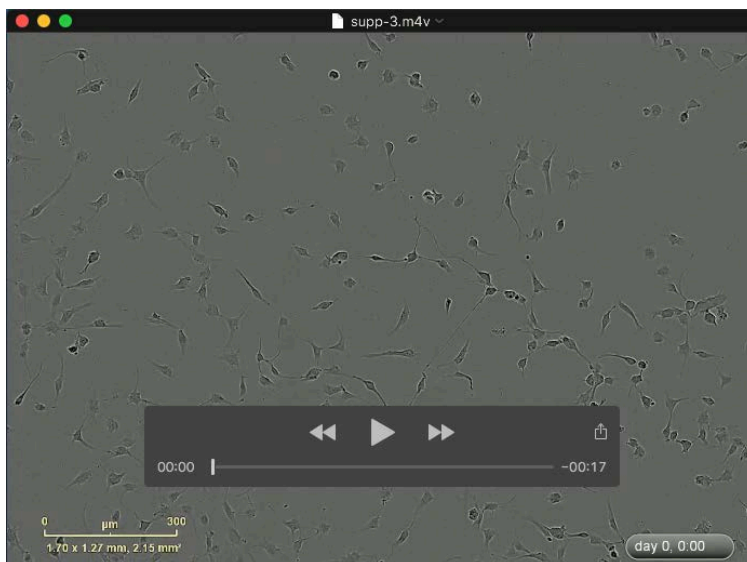


Fig. S4. Nuclear damage in the iNet phenotypic conditions was associated with the non-connected cellular subpopulation of total iNet cells. (A) GBM1 cells in iNet conditions were exposed to the indicated radiation doses and pie charts depict the percentages of fragmented nuclei 5 days post radiation treatment. (B) GSEA plots of ranked gene expression (FDR <5%) comparing transcriptional iNet and Rev profiles upon 20 Gy radiation and their positive (red) and negative (blue) correlations for the indicated gene sets. Enrichment scores are shown as green lines, and the horizontal black bars indicate the position of associated genes for each gene set. Plots suggest that the iNet RNA expression was positively-correlated with the indicated Gene Ontology Consortium (GO, Ashburner et al. 2000; The Gene Ontology Consortium 2017) and HALLMARK pathways (Liberzon et al. 2015) as compared with the negatively-correlated Rev phenotype profile in GBM1 cells.

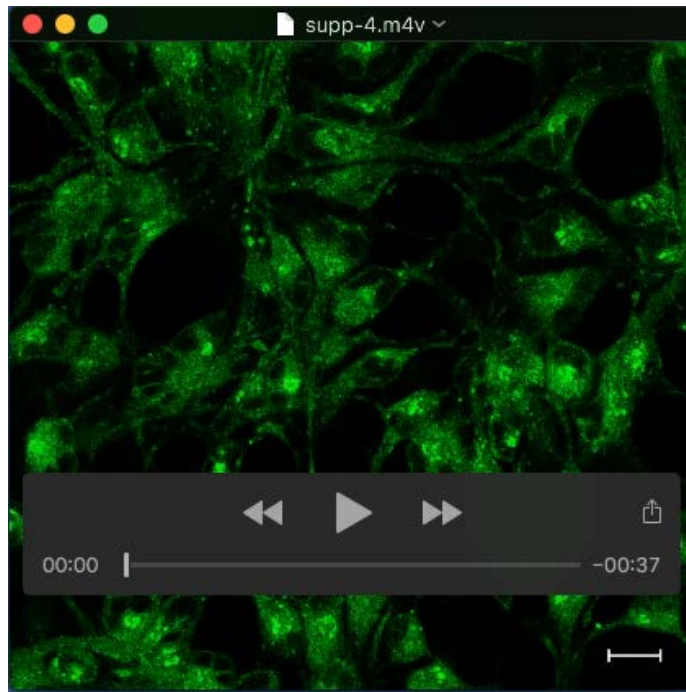
SUPPLEMENTAL MOVIES



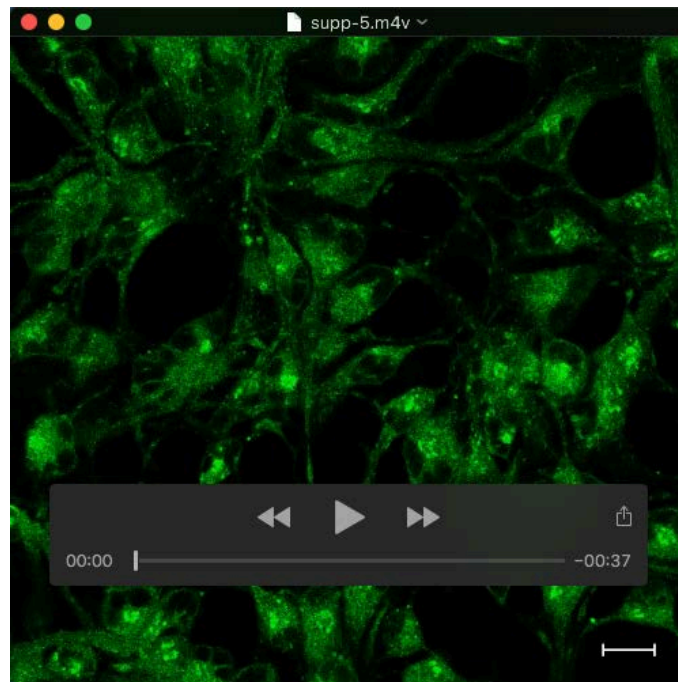
Movie 1. GBM1 cell model, vehicle (H₂O) treatment, time lapse period: 24 hours.



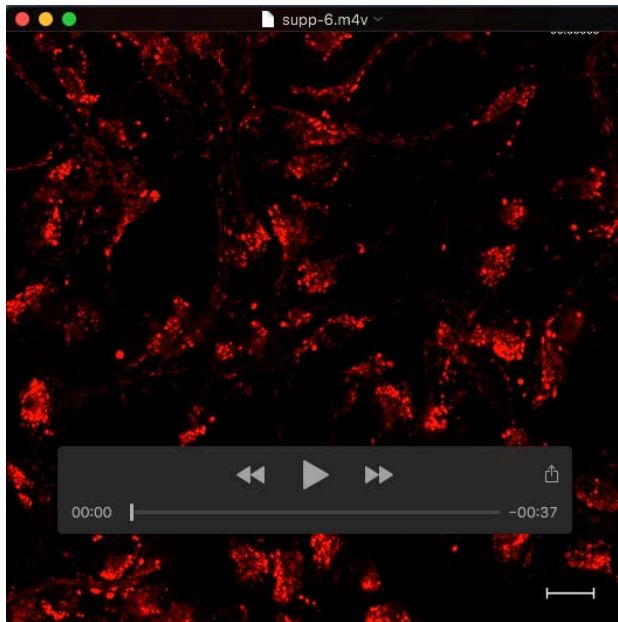
Movie 2. GBM1 cell model, Y-27632 (20 μ M) treatment, time lapse period: 24 hours.



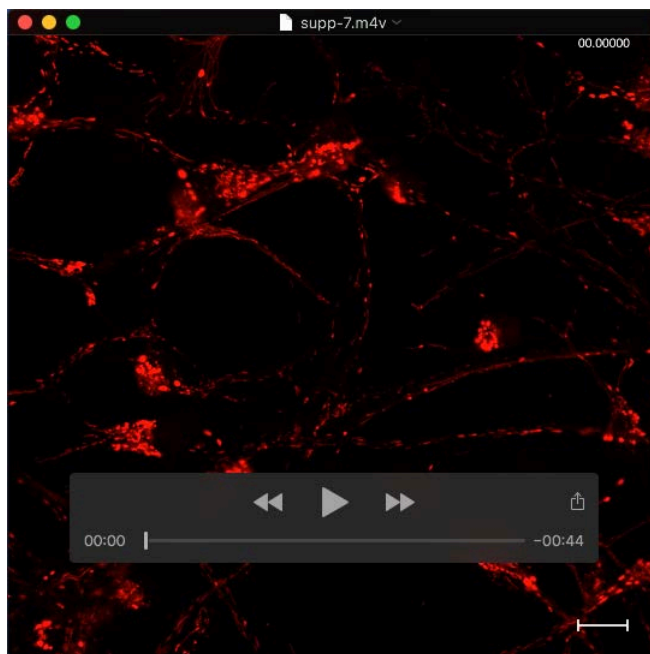
Movie 3. GBM1 cell model, Con phenotype, Mitotracker labelling (red), time lapse period: 30 minutes. Scale bar, 20 μ m.



Movie 4. GBM1 cell model, iNet phenotype, Mitotracker labelling (red), time lapse period: 30 minutes. Scale bar, 20 μ m.



Movie 5. GBM1 cell model, Con phenotype, Lysotracker labelling (green), time lapse period: 30 minutes. Scale bar, 20 μm .



Movie 6. GBM1 cell model, iNet phenotype, Lysotracker labelling (green), time lapse period: 30 minutes. Scale bar, 20 μm .